Materials Research Proceedings 28 (2023) 219-230 https://doi.org/10.21741/9781644902479-24

Modeling of 3D fluid-structure-interaction during in-situ hybridization of double-curved fiber-metal-laminates

POPPE Christian[1,3,a], KRUSE Moritz[2,b] and KÄRGER Luise[1,c *]

[1]Karlsruhe Institute of Technology (KIT), Institute for Vehicle System Technology (FAST), Institute Division Lightweight Design, Germany

[2]Institute for Production Technology and Systems, Leuphana University of Luneburg, Germany

[3] Simutence GmbH, Germany

[a]christian.poppe@partner.kit.edu, [b]moritz.kruse@leuphana.de, [c] luise.kaerger@kit.edu

Keywords: Composites, Process Simulation, Infiltration, Deep Drawing, FML, FSI, FEA

Abstract. Fiber-metal-laminates (FML) provide excellent fatigue behavior, damage-tolerant properties, and inherent corrosion resistance. A 2017-developed single-step process that combines deep-drawing with simultaneous infiltration (in-situ-hybridization) yields promising results. However, Fluid-Structure-Interaction (FSI) between the hybrid stack and the fluid pressure complicated the defect-free processing of double-curved parts. In this work, a Finite Element (FE) simulation approach for modeling the in-situ hybridization of FMLs is expanded to incorporate a both-sided (strong) FSI, aiming to facilitate apriori virtual support for process- and part development. Using Terzaghi's effective stress formulation, the proposed framework can predict metal sheet buckling and resin accumulation resulting from local fluid pressure during infiltration of the textile interlayers on part level. Different conditions are simulated, outlining the high relevance of considering strong FSI during process simulation. The part-level results are compared with experimental findings. Modeling challenges are discussed, along with suggested future enhancements of the simulation approach.

Introduction

The aerospace industry has driven the processing and application of Fiber Metal Laminate (FML) in recent decades [1,2]. Combining the best features of metals and composite materials, FML provides excellent fatigue behavior, damage-tolerant properties, inherent corrosion resistance, and good fire resistance [3,4]. Product examples are GLARE (Glass-Fiber Reinforced Aluminum Laminates) or ARALL (Aramid-Reinforced Aluminum Laminates). Beyond flat structures, defect-free manufacturing of three-dimensional curved FMLs with a high degree of automation still proves difficult and is extensively investigated in the literature [1,5, 6]. Despite experimental trials, several numerical models with varying focus and scale have been proposed and validated, enabling a prediction of potential wrinkling, fracture, or strains with metal sheets or fibers [6–10]. A strong FSI during in-situ hybridization has not been modeled so far. The classical manufacturing process using an autoclave is time-consuming, expensive, and the achievable geometric complexity of the components is very low [11]. In this regard, Mennecart et al. [12] suggested and developed, among others [13,14], an alternative manufacturing process by combining deep drawing with thermoplastic resin transfer molding, called hybrid liquid composite molding (HyLCM).

A schematic illustration of the principal process steps is given in Fig. 1. The stack is positioned between a matching punch and a die. The stack is clamped during the whole process using circumferential blank holders. In the first step, the hybrid stack is only slightly deformed, temporarily sealing the outer rim. Subsequently, reactive resin is centrally injected through a hole in the lower metal layer while deep drawing proceeds. The fluid pressure can bend the metal top

layer during injection, as illustrated in Fig. 1. During the last 20% of the tool stroke, the resin is forced outward and infiltrates the core GF layers. The heated molds enforce isothermal curing.

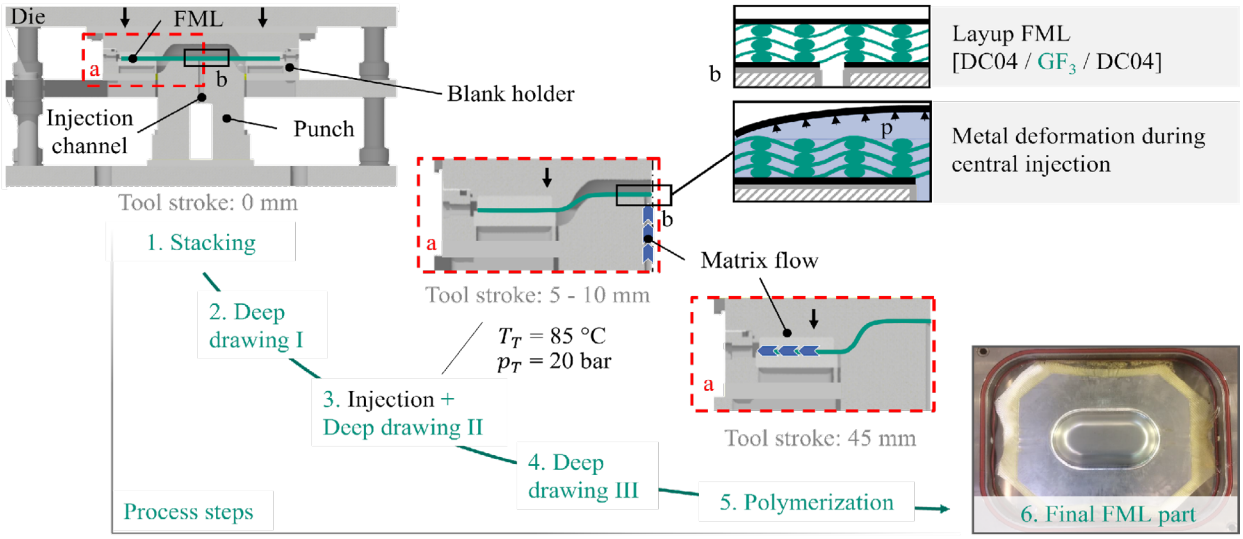

*Fig. SEQ Figure * ARABIC 1. Visualization of the combined deep-drawing and LCM process (HY-LCM) from Stacking (1.) to intermediate injection (3.) and final polymerization*

Objective

In a previous work [10], the authors presented a macroscopic process simulation model for the outlined process, which allows modeling the deep drawing of the FML stack, including transverse compression of the textile core layers and the simultaneously arising fluid progression. The deep-drawing model was verified with close-to-process trials. However, the presented model only incorporated a weak Fluid-Structure-Interaction (FSI). Local deformation was considered during fluid progression, but fluid pressure-related deformation was neglected.

As experiments and available literature show that an accurate prediction of potential defects requires modeling a strong FSI, this paper aims to implement and investigate a both-sided coupling between FML material deformation and fluid progression.

Exemplary Processing Results

Process trials are conducted at Leuphana University Lüneburg (Germany) with different parameter settings combining two DC04 metal sheets (1 mm) with six core layers made from a glass twill fabric (280 g/m^2, INTERGLAS 92125 FK800) [15]. A thermoplastic matrix (Arkema Elium® 150), with an initial viscosity of 100 mPas, mixed with 2.5 % hardener, is injected.

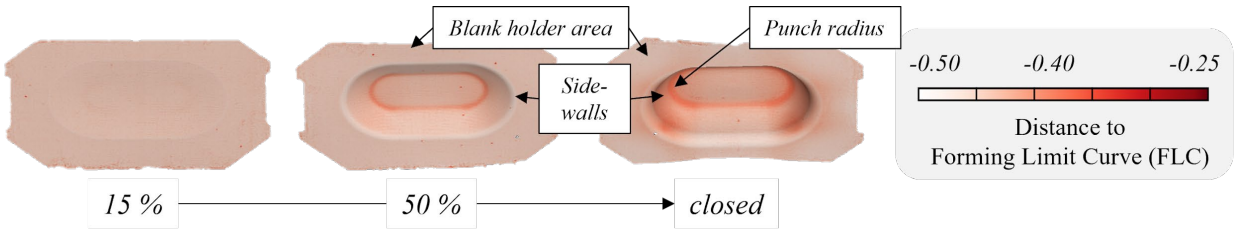

Fig. 2. Shaping and distance to the Forming Limit Curve, data obtained with GOM ARGUS measurements.

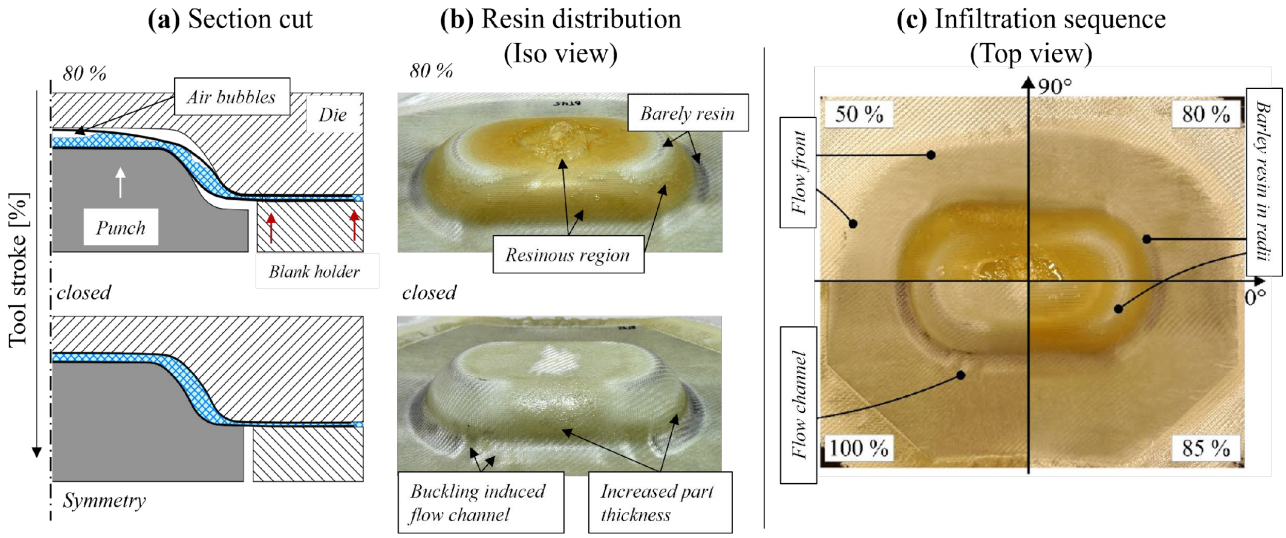

Fig. 3. Visualization of the FSI during FML processing; (a) Schematic section cut; (b) Photos illustrating the resin distribution; (c) Infiltration sequence and observed effects.

Fig. 2 summarizes a shaping of a part during the tool stroke and the distance to the Forming Limit Curve (FLC). The distance to the FLC indicates forming margin before failure. During dry forming trials, the FML stack is deep-drawn without buckling, as no additional fluid pressure is present, and other parameters are adjusted suitably. This changes when injecting the reactive resin. Driven by the fluid pressure between the metal sheets, bending of the metal sheet is observed close to the injection port and later towards the side walls of the geometry.

These observations are schematically illustrated in more detail in Fig. 3 (a,b). The resin first accumulates between the metal sheets, especially near the inlet and the side walls. The blank holder seals this region and prevents fluid-induced deformation in the flange area. Fig. 3 (b,c) shows that the fluid is forced through the flange during subsequent tool closure. Fluid is pushed out of the bottom area and other regions where high compressive stress is induced by the deep drawing of the metal, such as the punch radius or the side walls. These exemplary results illustrate the high relevance of strong FSI modeling for reliable virtual product- and process design for in-situ hybridized FMLs.

Process Simulation Model

This work's applied process simulation model originates from WCM modeling [16, 17], which has been expanded and verified to account for hybrid FML forming and weak FSI [10]. A schematical overview of the macroscopic FE-based simulation framework is given in Fig. 4.

Two fully-coupled submodels provide the core part of the model to describe the intra-ply behavior of the textiles (a). The FE-based draping submodel captures the macroscopic deformation mechanism, such as membrane, bending, or compaction behavior. A superimposed FE/CV-based fluid submodel describes the fluid progression and pressure field using Darcy's law for porous media flow. This approach implies that the fluid is modeled homogenized and purely liquid regions cannot be modeled discretely. Both submodels are formulated three-dimensionally, enabling a local prediction of fiber orientation, FVC, and modeling of squeeze flow as well as infiltration in the thickness direction. Despite that, the framework comprises a material model for the metal sheets, see Fig. 4b, and an interface model which describes the dry and infiltrated contact behavior during processing (cf. Fig. 4c).

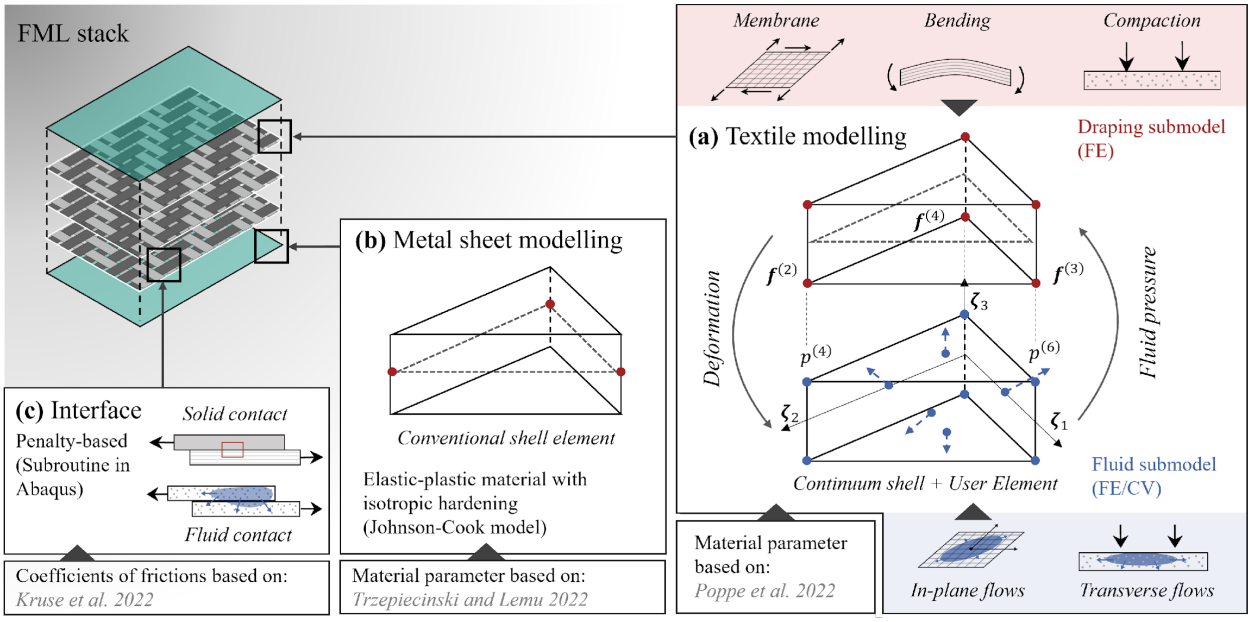

Fig. 4. Process simulation modelling framework in ABAQUS, clustered according to interface, metal sheet and textile modelling.

Draping submodel.

The relevant deformation modes of the glass fiber textile are in-plane shearing (membrane), out-of-plane bending, and compaction. They are implemented through a superimposed reduced-integrated continuum shell (SC6R) and a hyper-elastic material formulation (St. Venant-Kirchhoff material) in a thickness direction within a user element, see Fig. 4a. This approach neglects the required decoupling between the membrane and bending behavior [16]. In the case of the FML modeling, an overestimated bending stiffness can be accepted as the bending stiffness of the stack is dominated by the metal sheets. For a description of transverse compaction modeling, including identified material parameters, the reader is referred to our last year's contribution [10].

The hypervisco-elastic in-plane *membrane model* [18] has not been explicitly characterized for the here applied glass fiber textile. Yet, its prediction on the here-applied geometry has been compared to a membrane model designed for the used material [19]. A pre-study showed comparable fiber orientation, which is reasonable as the geometry is relatively simple and does not induce defects or shear looking. The former model was chosen as it proved more robust in combination with active strong FSI.

A transverse shear stiffness of $\kappa_{GF,11}, \kappa_{GF,22} = 1.0$ N/mm² is used to adapt the *out-of-plane bending* stiffness within the continuum shell. Based on these parameters and the underlining

Materials Research Proceedings 28 (2023) 219-230 https://doi.org/10.21741/9781644902479-24

membrane model, the model overestimates the textile's bending stiffness by approximately 100. However, compared to the bending stiffness supplied by the metal sheets, the bending stiffness of the textile is negligible.

Fluid submodel.

Darcy's law, in combination with mass conservation, is applied in a transient explicit formulation and is embedded in the superimposed user element (cf. Fig. 4a) to solve the pressure field and model flow front progression [17]

$$\int_{V_k} \rho C_{hyd}\, \dot{p}\; dv = \frac{\boldsymbol{K}(\phi)}{\eta \cdot \varphi} \int_{V_k} \mathrm{div}(\mathrm{grad}(p) - \rho g)\, dv \tag{1}$$

Using Eq. 1, a transient single-phase flow based on an explicit time integration scheme can be modeled. Here, $K(\phi)$ is the permeability tensor as a function of the current FVC ϕ. The viscosity is given by η, and $\varphi = 1 - \phi$ is the porosity.

The in-plane permeability values are given by

$$K_{11}(\phi) = 0.009 \cdot e^{-11.3 \cdot \phi}, K_{22}(\phi) = 0.004 \cdot e^{-11.8 \cdot \phi}, K_{33}(\phi) = 0.01 \frac{K_1(\phi) + K_2(\phi)}{2}, \tag{2}$$

and the permeability in the thickness direction, which has not been measured for the material yet, is estimated using a downscaling factor of 100 based on the results of a comparable material [20]. This estimation in the thickness direction is not a critical assumption as the fluid is contained between the sheets, and pressure-relevant flows are in-plane.

Based on the pressure field within the saturated domain, fluid progression is implemented using the flows across every element surface at the flow front in combination with element-based saturation values. The saturation values are updated in every increment, and saturated elements are added to the transient domain governed by Eq. 1.

Strong FSI.

To this point, a one-sided (weak) FSI is presented in the model as the deformation drives the pressure field and fluid progression in the textile. Terzaghi's effective stress, according to MacMinn et al. [21], is implemented to consider the fluid pressure and drag forces acting on the porous medium. As Eq. 3 shows, this yields two new nodal force terms that add up with the material reaction forces.

$$\hat{\boldsymbol{f}}_{\mathrm{R}}^{\mathrm{Node}} = \hat{\boldsymbol{f}}_{\mathrm{R}}^{\mathrm{Mat}} + \hat{\boldsymbol{f}}_{\mathrm{R}}^{\mathrm{p}} + \hat{\boldsymbol{f}}_{\mathrm{R}}^{\mathrm{d}} \quad \text{with } \hat{\boldsymbol{f}}_{\mathrm{R}}^{\mathrm{p}} = -\det(\boldsymbol{J})\, p \boldsymbol{I} \quad \text{and} \quad \hat{\boldsymbol{f}}_{\mathrm{R}}^{\mathrm{d}} = \det(\boldsymbol{J})\, \varphi \boldsymbol{N}\, \mathrm{grad}(p) \tag{3}$$

The first one represents the reaction forces $\hat{\boldsymbol{f}}_{\mathrm{R}}^{\mathrm{p}}$ caused by the fluid pressure within the skeleton structure of the deformable porous medium, and the second one representing the fluid drag $\hat{\boldsymbol{f}}_{\mathrm{R}}^{\mathrm{d}}$ between flow and fabric. In Eq. 3, $\boldsymbol{I}$ is the second-order unit tensor, and $\boldsymbol{N}$ represents the element shape function. Using the permeability values in Eq. 2, the method can be applied to the glass woven fabric without further adjustments. This formulation has been validated in [22].

Metal sheet.

The model comprises an elastic-plastic material model with isotropic hardening based on the built-in Johnson-Cook model for the metal sheets using conventional shell elements with a constant thickness (cf. Fig. 4) parameterized by Trzepiecinski and Lemu [23] for the same material. A comparison between experiments and the simulation on a single metal sheet yields a good agreement of the obtained reaction forces and deformations [10].

Interface. Contact behavior between ply and tool interfaces is modeled using penalty-based contact algorithms in ABAQUS/explicit, cf. Fig. 4. In the case of dry friction (solid contact), coulomb friction is modeled using coefficients of friction (CoF) that have been identified by Kruse et al. [24] ($\mu_{Tool,Metal}$ = 0.2, $\mu_{Tool,Textile}$= 0.253, $\mu_{Textile,Textile}$= = 0.334). Due to the metal sheet, high contact stresses of 2000 N/mm^2 are necessary to prevent excessive contact penetration. A damping of 1 N/s mm is used to reduce contact oscillations. In case of an infiltrated contact, hydrodynamic friction is used in combination with maximal tangential contact stress of $\tau_{t,max} = 1 \cdot 10^{-4}$ N/mm². Arising contact slips of several millimeters prevented the proper usage of cohesive zones during draping.

Small-Scale Application

Before part-level application, the outlined simulation approach is applied to a small slice of the final geometry to investigate the impact of infiltration during a processing sequence, see Fig. 5 (a,b). Similar to the physical process (cf. Fig. 1), an initial dry deep drawing phase is followed by a central injection phase within further punch movement, see Fig. 5c. Afterward, the partly pre-infiltrated stack is draped into the final shape without additional injection.

The tools are modeled as rigid surfaces, and displacement boundary conditions drive the blank holder and the punch. The stack is modeled as outlined above. The three textile core layers are homogenized into a single instance with an initial thickness of 1.2 mm. A constant pressure of 5 bar is applied to the inlet nodes between 0.5 and 4 seconds. Each metal sheet has an initial thickness of 0.5 mm. The tool geometry is derived from a deep-drawing configuration, resulting in a non-constant cavity in the closed state. A velocity of 100 mPas is assumed.

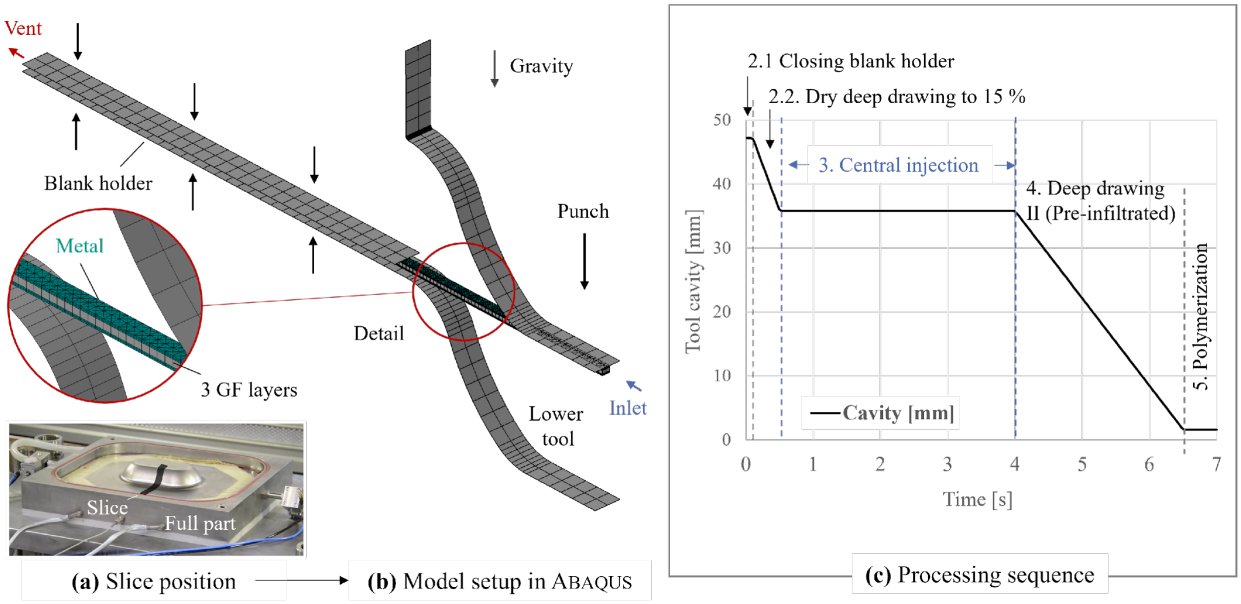

Fig. 5. Small scale demonstrator: (a) Slice position; (b) Setup and (c) Processing sequence.

To assess the impact of fluid progression along with strong FSI during processing, Fig. 6a comprises results for a dry deep-drawing reference. It shows that during a solely dry forming, the fabric layers are squeezed between the metal sheets, leading to significant compaction in the thickness direction below the blank holder and on the radii (cf. Fig. 6a). As deep-drawing of the metal sheets induces substantial in-plane strains, the textile layers are also compressed in the not

directly contacted side-wall region, recall Fig. 2. Consequently, the cavity is not entirely occupied by the FML laminate after the tool has closed completely.

Considering the injection and resulting FSI between fluid pressure and FML stack, see Fig. 6b, allows for predicting the above-made experimental observations. Injection leads to a severe increase in stack thickness towards the inlet. During the pre-infiltrated deep-drawing face (4.), the resin is forced through the side wall regions and eventually the blank holder. The fluid pressure prevents comparable high FVCs during processing and enforces a more homogeneous distribution. In this regard, the average FVC for the dry setup is predicted at 51.3 %, compared to only 40 % in the case of strong FSI consideration.

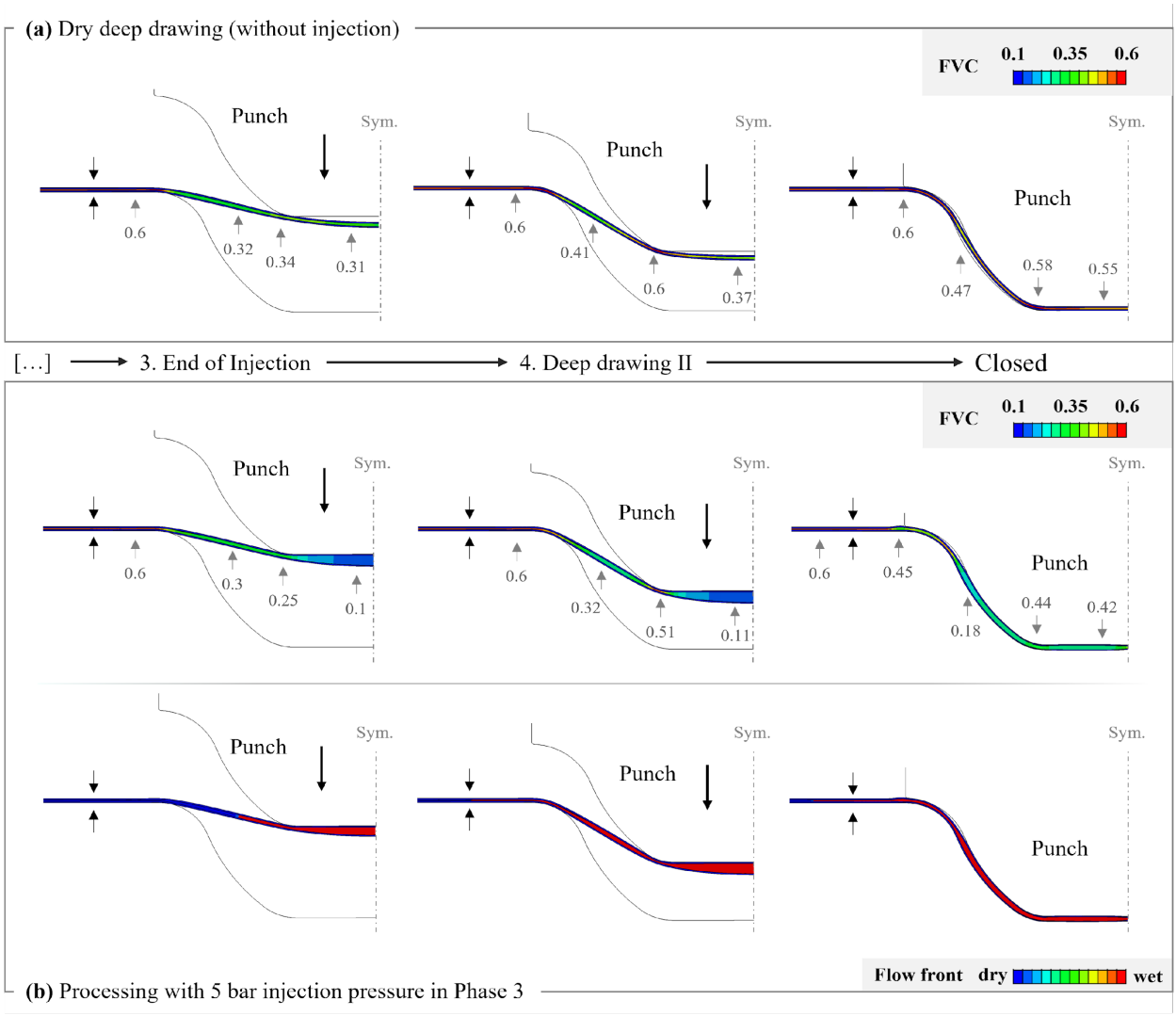

Fig. 6. Small demonstrator results: (a) Dry conditions; (b) Conditions according to Fig. 5 (c).

Part-scale Application

Finally, the outlined model is deployed on part level using the same geometry as for the physical process illustrated in Fig. 1. The modeling setup, comprising the FML stack, punch, lower tool, and blank holder, is shown in Fig. 7. Model settings are identical to the small-scale simulation trials, yet the simulation starts with a pre-saturated area, not matching the exact processing sequence, see Fig. 7b.

This adaption was necessary to reduce the required computational effort. The nonlinearity of implemented, interacting physical effects and the substantial stiffness differences between the fabric layers and the metal sheet requires a relatively small stable time increment during time integration in ABAQUS/explicit. A fluid amount of 100 ml is prescribed for the model (100 mPas). The outlined setup is simulated with both configurations to assess the impact of a one-sided (weak) and a both-sided (strong) FSI. The comparison of predicted punch reaction forces in Fig. 7 shows that significant differences only arise within the last 30% of the tool stroke when the available space of the metal sheets to evade the fluid pressure reduces to the cavity.

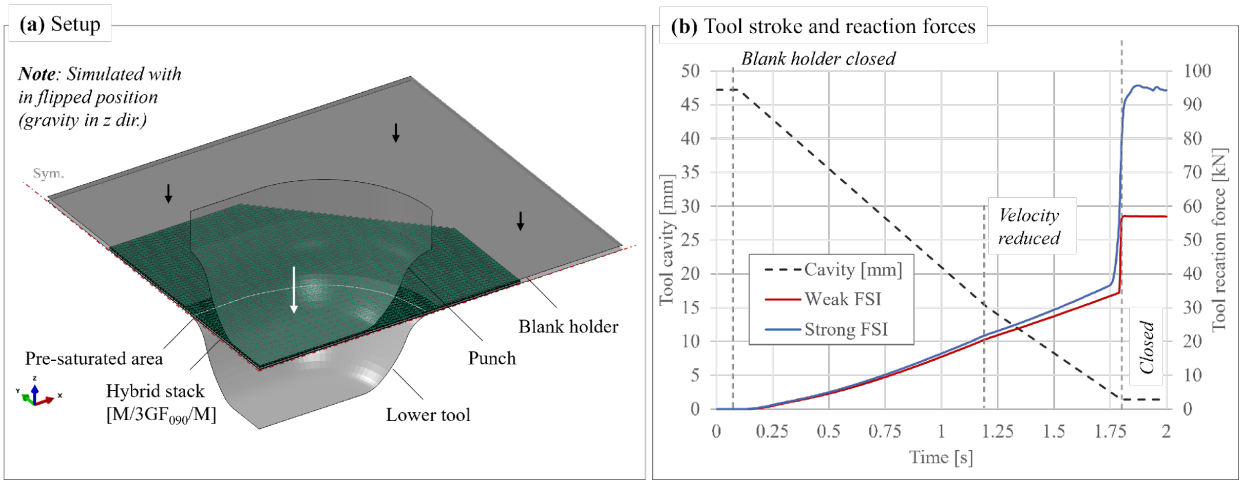

Fig. 7. Process simulation on part level; (a) Setup and (b) Tool stroke and obtained reaction forces during partly pre-infiltrated conditions using weak or strong FSI settings.

In contrast, significant differences arise early during processing when comparing the spatial distribution of the flow front, see Fig. 8, and the resulting FVC (cf. Fig. 9). Due to the local increase in the part thickness, less fluid is pushed toward the circumferential blank holder region. As a result, the flow front progression is overpredicted by the weak FSI approach.

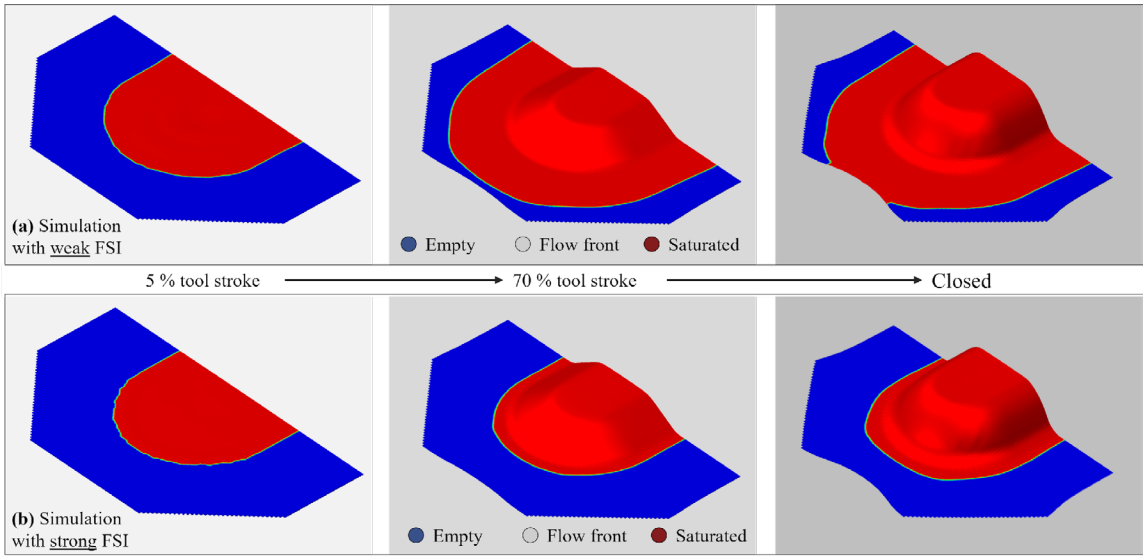

Fig. 8. Impact of FSI on flow front progression: (a) One-sided (weak) FSI, fluid pressure is not considered; (b) Both-sided (strong) FSI, fluid pressure leads to material deformation.

Fig. 9 summarizes the resulting FVC distribution and thickness for different regions of the geometry during 25, 70, and 100 % of the tool stroke. Regarding FSI consideration, comparable interactions to the small-scale demonstrator are present. As before, the compaction of the fabric results in increased part thickness in regions not directly contacted by the tool surfaces. This applies to both configurations.

Moreover, strong FSI increases the local stack thickness significantly as the fluid pressure beads the metal layers surrounding the fabric stack. Consequently, severe differences are predicted already at 25 % during processing. These differences reduce towards the end of the tool stroke as the FML stack is squeezed into the cavity, yet the average FVC for the weak FSI configuration is still 4% higher (55.8 % weak, 51.8 % strong).

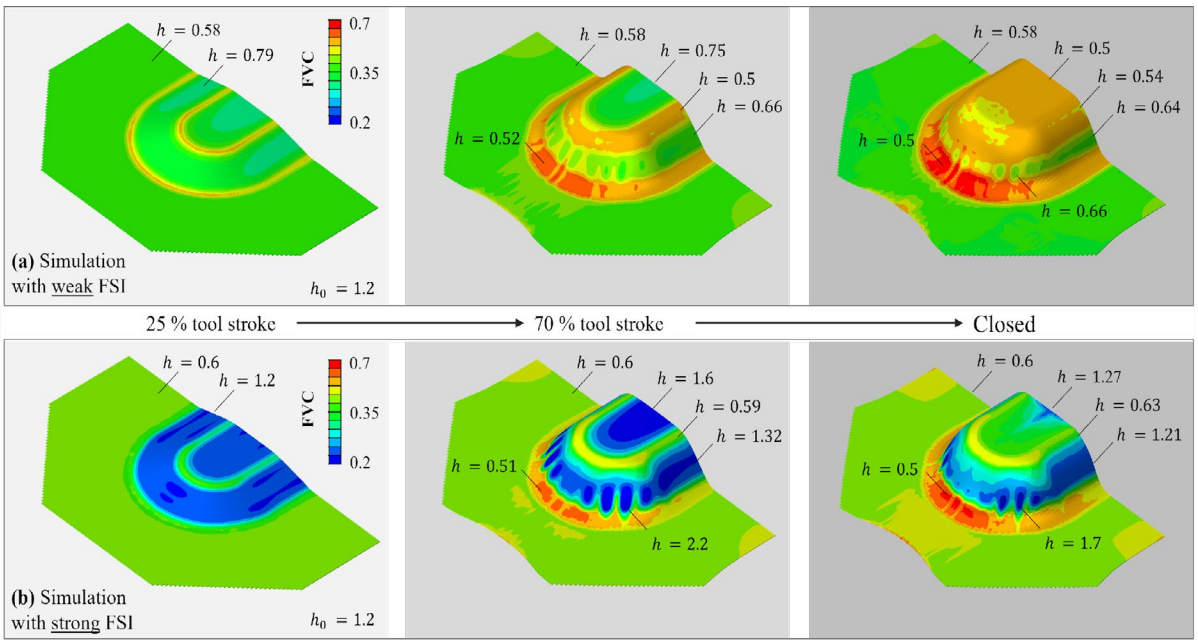

Fig. 9. Impact of FSI on FVC and part thickness (h) during partly pre-infiltrated forming.

Comparison with experiments.

Comparing the strong FSI results outlined in Fig. 8b and Fig. 9b with the above-introduced experimental observations, see Fig. 3, it becomes apparent that several effects can be predicted correctly. Although the single-phase-based modeling approach cannot predict pure resin areas, it can give a good prediction of where fluid accumulates during forming and in the final state. Moreover, fully-coupled interaction modeling between fluid, fabric, and metal sheets allows for predicting the onset of buckling of the metal sheets in the corners of the dome geometry. This buckling leads to flow channels similar to experimental observations, reducing the area's local FVC.

Summary

A fully-coupled macroscopic process simulation model for modeling producing in-situ hybridized, double-curved FML is presented. Experimental observations in the literature and on the here investigated FML process indicate a strong interaction between fluid pressure and forming of the FML stack. Reported defects such as buckling of the metal sheets, dry spots, or resin accumulations in corners could not be comprehensively numerically predicted so far, which hinders process- and part development.

Using an FE-based simulation approach combined with a control volume-based fluid progression model, the arising FSI can be considered directly via additional nodal reaction forces at the element nodes. Simulation trials on a slice of the actual geometry comparing a solely dry configuration with one that matches the processing sequence, including central injection, underline the importance of considering strong FSI in process simulation. Simulations on the part level confirm these observations and show that the simulation approach can predict the experimentally identified effects, such as resin accumulation and metal sheet buckling.

Outlook

For now, a relatively small time increment of 1E-07 is necessary to stabilize the simulation, resulting in substantial computation times on the part level. An improved interface modeling technique and stable time increment algorithm are assumed to improve the model's performance. Beyond that, a two-phase flow model would allow for predicting air entrapments and resin-rich regions. However, a two-phase model presumably requires a non-monlytic approach by coupling a proper-fluid solver with the proposed draping submodel. Heat transfer and resin kinetics should also be implemented into the proposed framework to increase prediction accuracy and support process parameter identification.

Acknowledgments

The authors would like to thank the German Research Foundation (DFG) for funding the projects BE 5196/4-1 and BE 5196/4-2. Moreover, the authors would like to thank the German Federal Ministry of Education and Research (BMBF) for the funding of the project" HyWet" (03INT614AC) as part of the Transatlantic Cluster for Lightweighting (TraCLight), for which some presented numerical methods were developed. This work is also part of the Young Investigator Group (YIG)" Tailored Composite Materials for Lightweight Vehicles", gratefully funded by the Vector Stiftung.

References

[1] Z. Ding, H. Wang, J. Luo, N. Li, A review on forming technologies of fibre metal laminates, Int. J. Lightweight Mater. Manuf. 4 (2021) 110-126. https://doi.org/10.1016/j.ijlmm.2020.06.006
[2] S. Krishnakumar, Fiber Metal Laminates – The Synthesis of Metals and Composites, Mater. Manuf. Process. 9 (1994) 295-354. https://doi.org/10.1080/10426919408934905
[3] A. Asundi, A.Y. Choi, Fiber metal laminates: an advanced material for future aircraft, J. Mater. Process. Technol. 63 (1997) 384-394. https://doi.org/10.1016/S0924-0136(96)02652-0

[4] M.R. Sadeghi, A.A.A. Jeddi, S. Shaikhzadeh Najar, Theoretical and ezperimental analysis of bending rigidity of plain and twill woven fabrics, J. Text. Inst. 108 (2017) 1700. http://doi.org/10.1080/00405000.2017.1280760
[5] T. Sinmazçelik, E. Avcu, M.Ö. Bora, O. Çoban, A review: Fibre metal laminates, background, bonding types and applied test methods, Mater. Design 32 (2011) 3671-3685. https://doi.org/10.1016/j.matdes.2011.03.011
[6] M. Smolnicki, G. Lesiuk, S. Duda, A.M.P. de Jesus, A Review on Finite-Element Simulation of Fibre Metal Laminates, Arch. Computat. Methods Eng. 1 (2022). https://doi.org/10.1007/s11831-022-09814-8
[7] H. Blala, L. Lang, S. Khan, S. Alexandrov, Experimental and numerical investigation of fiber metal laminate forming behavior using a variable blank holder force Prod. Eng. Res. Devel. 14 (2020) 509. https://doi.org/10.1007/s11740-020-00974-9
[8] H. Blala, L. Lang, L. Li, S. Alexandrov, Deep drawing of fiber metal laminates using an innovative material design and manufacturing process, Compos. Communic. 23 (2021) 100590. https://doi.org/10.1016/j.coco.2020.100590
[9] L. Li, L. Lang, B. Hamza, Q. Zhang, Effect of hydroforming process on the formability of fiber metal laminates using semi-cured preparation, Int. J. Adv. Manuf. Technol. 107 (2020) 3909–3920. https://doi.org/10.1007/s00170-020-05281-2
[10] C.T. Poppe, H.O. Werner, M. Kruse, H. Chen, N. Ben Khalifa, F. Henning, L. Kärger, Towards 3D Process Simulation for In Situ Hybridization of Fiber-Metal-Laminates (FML), Key Eng. Mat.926 (2022) 1399-1412. https://doi.org/10.4028/p-cr2tco
[11] J. Sinke, Manufacturing of GLARE Parts and Structures, Appl. Compos. Mater. 10 (2003) 293–305. https://doi.org/10.1023/A:1025589230710
[12] T. Mennecart, S. Gies, N. Ben Khalifa, A.E. Tekkaya, Analysis of the Influence of Fibers on the Formability of Metal Blanks in Manufacturing Processes for Fiber Metal Laminates, J. Manuf. Mater. Process. 3 (2019) 2. https://doi.org/10.3390/jmmp3010002
[13] B.-A. Behrens, S. Hübner, N. Grbic, M. Micke-Camuz, T. Wehrhane, A. Neumann, Forming and Joining of Carbon-Fiber-Reinforced Thermoplastics and Sheet Metal in One Step, Procedia Eng. 183 (2017) 227-232.
[14] Y. Lu, Y. Li, Y. Zhang, L. Dong, Manufacture of Al/CF/PEEK curved beams by hot stamping forming process, Mater. Manuf. Process. 1 (2022) 1597-1609. https://doi.org/10.1080/10426914.2022.2032140
[15] M. Gerdes, Experimental mold filling analysis and investigation of the forming behavior during deep drawing of fiber-metal laminates in the in-situ hybridization process, Master Thesis, Lueneburg, 2022.
[16] P. Boisse, R. Akkerman, P. Carlone, L. Kärger, S.V. Lomov, J.A. Sherwood, Advances in composite forming through 25 years of ESAFORM, Int. J. Mater. Form. 15(3) (2022). https://doi.org/10.1007/s12289-022-01682-8
[17] C.T. Poppe, C. Krauß, F. Albrecht, L. Kärger, A 3D process simulation model for wet compression moulding, Compos. Part A: Appl. Sci. Manuf. 145 (2021) 106379. https://doi.org/10.1016/j.compositesa.2021.106379
[18] C.T. Poppe, D. Dörr, F. Henning, L. Kärger, Experimental and numerical investigation of the shear behaviour of infiltrated woven fabrics Compos. Part A: Appl. Sci. Manuf. 114 (2018) 327-337. https://doi.org/10.1016/j.compositesa.2018.08.018
[19] F. Schäfer, H.O. Werner, F. Henning, L. Kärger, Compos. Part A: Appl. Sci. Manuf. 165 (2022) 107323. https://doi.org/10.1016/j.compositesa.2022.107323
[20] C.T. Poppe, Process simulation of wet compression moulding for continuous fibre-reinforced polymers, KIT Scientific Publishing, Karlsruhe, 2022.

[21] C.W. MacMinn, E.R. Dufresne, J.S. Wettlaufer, Large deformations of a soft porous material, Phys. Rev. Appl. 5 (2016) 044020. https://doi.org/10.1103/PhysRevApplied.5.044020
[22] C.T. Poppe, F. Albrecht, C. Krauß, L. Kärger, Towards numerical prediction of flow-induced fiber displacements during wet compression molding (WCM), Paper presented at ESAFORM 2021. 24th International Conference on Material Forming, Liège, Belgique, 2021. https://doi: 10.25518/esaform21.1938
[23] T. Trzepiecinski, H. Lemu, Effect of Computational Parameters on Springback Prediction by Numerical Simulation, Metals 7 (2017) 380. https://doi.org/10.3390/met7090380
[24] M. Kruse, H.O. Werner, H. Chen, T. Mennecart, W.V. Liebig, K.A. Weidenmann, N. Ben Khalifa, Investigation of the friction behavior between dry/infiltrated glass fiber fabric and metal sheet during deep drawing of fiber metal laminates, Prod. Eng. Res. Devel. 17 (2022) 37-46. https://doi.org/10.1007/s11740-022-01141-y